Advances in Materials Physics and Chemistry, 2019, 9, 175-198
https://www.scirp.org/journal/ampc
ISSN Online: 2162-5328
ISSN Print: 2162-531X

Structural, Magnetic, and Electrical Properties of RE Doped $Sr_{0.82}RE_{0.18}Fe_{12-x}Al_xO_{19}$ (RE = Gd, Pr, Sm) Compound

Dom Lal Kunwar[1,2*], Dipesh Neupane[1,3], Jiba Nath Dahal[1,4], Sanjay R. Mishra[1]

[1]Department of Physics and Material Science, The University of Memphis, Memphis, TN, USA
[2]Department of Physics, Kent State University, Kent, OH, USA
[3]Department of Engineering Technology, The University of Memphis, Memphis, TN, USA
[4]Department of Physics, Truman State University, Kirksville, MO, USA
Email: *dkunwar@kent.edu

How to cite this paper: Kunwar, D.L., Neupane, D., Dahal, J.N. and Mishra, S.R. (2019) Structural, Magnetic, and Electrical Properties of RE Doped $Sr_{0.82}RE_{0.18}Fe_{12-x}Al_xO_{19}$ (RE = Gd, Pr, Sm) Compound. *Advances in Materials Physics and Chemistry*, **9**, 175-198.
https://doi.org/10.4236/ampc.2019.99014

Received: July 3, 2019
Accepted: September 16, 2019
Published: September 19, 2019

Abstract

Among the family of ferrites, M-type hexaferrites has many industrial applications ranging from simple magnets to microwave devices. Improvement in magnetic and dielectric properties of ferrites is of continuous interest. In this present work details study is done to observe the effect of co-doping of rare-earth (RE^{3+}: Pr^{3+}, Sm^{3+}, and Gd^{3+}) and aluminum in $Sr_{0.82}RE_{0.18}Fe_{12-x}Al_xO_{19}$ (x = 0.0, 0.5, 1.0, 1.5, 2.0). The adopted samples were synthesized via autocombustion technique. Detailed synthesis, structural, magnetic, and electrical measurements of samples were performed to understand structural-magnetic-electrical property relationship. The Al^{3+} substitution for Fe^{3+} brings in a significant enhancement in coercivity but reduces magnetization due to the magnetic dilution effect. Additional coercivity enhancement was possible with RE^{3+} doping without affecting the magnetization of samples. Among all RE^{3+} doped samples, Pr^{3+} doped samples showed the highest Curie temperature, (T_c ~ 465˚C), while Gd^{3+} doped samples showed little variation in dielectric properties in GHz frequency range. This makes RE^{3+} doped samples as an ideal candidate for high-frequency microwave applications. Pr^{3+} with oblate charge distribution (negative Stevens constant) was observed to substitute well into the lattice consequently bringing in desired improvements in physical properties of $Sr_{0.82}RE_{0.18}Fe_{12-x}Al_xO_{19}$ ferrite.

Keywords

Sr-Ferrite, Nanocomposite, Magnetization, Curie Temperature, Coercivity, Dielectric Constant

1. Introduction

M-types hexagonal ferrites like $BaFe_{12}O_{19}$ and $SrFe_{12}O_{19}$ with magnetoplumbite structure have been widely investigated and used as a permanent magnet because of their high magnetization (M_s) and coercivity (H_c), low manufacturing cost for industrial production and stability [1] [2] [3]. Crystal structure of this magnetoplumbite is characterized by close packing of oxygen and Sr ions with Fe atoms at the interstitial positions. The hexagonal Sr-Ferrite has 24 Fe^{3+} ions per unit cell which are distributed on five different crystallographic sites viz. three octahedral sites, 12*k*, 2*a*, and 4*f*2, one tetrahedral site, 4*f*1, and one trigonal bipyramidal site, 2*b* [4]. Among them, three sites 12*k*, 2*a*, and 2*b* have spin-up, while 4*f*1 and 4*f*2 have spin down. Because of the competing effect of these spins, the ferromagnetic coupling is favored with the superexchange between Fe-O-Fe. Therefore, the distance between Fe-O-Fe becomes smaller. This lattice distortion leads to the situation where the magnetic moments of the five Fe sublattices are not mutually parallel. The magnetic structure is a collinear ferrimagnet with a net moment per unit cell of the only 40 μB at 4.2K [5]. It is known that Fe ions at 2*b* site provide the largest positive contribution to magnetic moment than at 4*f*1, 4*f*2, 2*a* (relatively weak and positive moments), 12*k* sites (negative moments) [6]. Hence, the intrinsic magnetic properties of Sr-Ferrite can be enhanced by substitution for Fe ions in different sites with other suitable ions. The intrinsic magnetic properties of Sr-hexaferrite are found to be affected by the partial substitution for Sr or Fe sites, or both. The different group reported significant improvement on magnetic properties by doping for Sr or Fe sites or both.

A significant improvement in magnetic properties has been reported in $SrFe_{12}O_{19}$ hexaferrites by the substitution of Sr^{2+} by rare-earth (RE^{3+}) ions such as by La^{3+} [7], Nd^{3+} [8], Sm^{3+} [9] [10], Gd^{3+} [11], Fe^{3+} ions by magnetic ions such as Co^{2+} [12] [13] and Cr^{3+} [14] ions and non-magnetic ions such as Al^{3+} [15], Zn^{3+} [16], Ga^{3+} [17] and Cd^{3+} [18] [19], and replacement of Sr^{2+}/Fe^{3+} together with Pr-Zn [20], La-Cu [21], and La-Zn [22]. From this reported literature on hexaferrites, it is observed that the insertion of RE^{3+} into hexaferrite lattice inhibits grain growth, reduces grain size, and thus controls the coercive force for wide practical applications. Recently our group has reported substantial enhancement in coercivity 300% in $SrFe_8Al_4O_{19}$ ferrite as compared to that of pure Sr-Ferrite [23]. The reported enhanced coercivity is attributed to the growth of monodomain particles. As ion size of the RE^{3+} element is smaller than Sr^{2+} (1.18 Å) [24], Fe^{3+} would be closer in the O-Fe-O lattice and a stronger interaction might be anticipated, which would result in changed magnetic properties in RE^{3+} ions doped Sr-Ferrite particles. Overall low concentration of RE^{3+} substitution for Sr^{2+} ion has been found effective in improving magnetization of Sr-Ferrite [25] [26]. So, proper substitution of magnetic RE^{3+} for Sr^{2+} and Al^{3+} for Fe^{3+} brings enhancement in coercivity of Sr-Ferrites [15] [23].

In the present work, we report the effect of co-doping RE^{3+}-Al^{3+} on magnetic and dielectric properties of $Sr_{0.82}RE_{0.18}Fe_{12-x}Al_xO_{19}$ (x = 0.0, 0.5, 1.0, 1.5, 2.0) na-

noparticles. The M-type $Sr_{0.82}RE_{0.18}Fe_{12-x}Al_xO_{19}$ ferrites were prepared via auto-combustion method. The process has the advantages of using inexpensive precursors, and the powders obtained are nanosized and homogeneous as compared to ferrites prepared via traditional solid-state reaction, a process which often leaves secondary phases in the compound [15].

2. Experimental

$Sr_{0.82}RE_{0.18}Fe_{12-x}Al_xO_{19}$ nanocomposite materials were prepared via a one-pot auto combustion method using nitrate salt. All the chemicals required for the synthesis were purchased from Sigma Aldrich. The stoichiometric weight of precursor used for the synthesis of $Sr_{0.82}RE_{0.18}Fe_{12-x}Al_xO_{19}$ composites is listed in **Table 1**. A stoichiometric amount of $RE(NO_3)_3{\cdot}6H_2O$, $Sr(NO_3)_2$, $Fe(NO_3)_3{\cdot}9H_2O$, and $Al(NO_3)_3{\cdot}9H_2O$ were dissolved in a minimum amount of deionized water (100 ml for 0.1 mol of Fe^{3+}) by stirring on a hotplate at 60˚C for 30 minutes. Citric acid was dissolved into the solutions to give a molar ratio of metal ions to citric acid of 1:1. NH_4OH was added dropwise to the solution until the pH value ~6.5 maintained. Then the solution was heated on a hotplate at 300˚C until gel ignites with the formation of large amounts of gas, resulting in lightweight voluminous powder. The resulting "precursor" powder was calcined at 950˚C for 12 hours to obtain pure $Sr_{0.82}RE_{0.18}Fe_{12-x}Al_2O_{19}$ hexaferrite powder.

Table 1. Details of the chemicals used for 1 g preparation of $Sr_{0.82}RE_{0.18}Fe_{12-x}Al_xO_{19}$.

	Weight (g)				
Pr doped Samples	$Sr(NO_3)_2$	$Pr(NO_3)_3{\cdot}6H_2O$	$Fe(NO_3)_3{\cdot}9H_2O$	$Al(NO_3)_3{\cdot}9H_2O$	Citric Acid
$Sr_{0.82}Pr_{0.18}Fe_{12}O_{19}$	0.16116	0.05684	4.5173	0.000	2.5454
$Sr_{0.82}Pr_{0.18}Fe_{11.5}Al_{0.5}O_{19}$	0.16391	0.05761	4.3854	0.1772	2.5803
$Sr_{0.82}Pr_{0.18}Fe_{11}Al_1O_{19}$	0.16618	0.05842	4.2558	0.3592	2.6162
$Sr_{0.82}Pr_{0.18}Fe_{10.5}Al_{1.5}O_{19}$	0.16853	0.05924	4.1195	0.5465	2.6528
$Sr_{0.82}Pr_{0.18}Fe_{10}Al_2O_{19}$	0.1706	0.05997	3.9716	0.7376	2.6856
Sm doped Samples	$Sr(NO_3)_2$	$Sm(NO_3)_3{\cdot}6H_2O$	$Fe(NO_3)_3{\cdot}9H_2O$	$Al(NO_3)_3{\cdot}9H_2O$	Citric Acid
$Sr_{0.82}Sm_{0.18}Fe_{12}O_{19}$	0.1618	0.07461	4.5226	0.000	2.5484
$Sr_{0.82}Sm_{0.18}Fe_{11.5}Al_{0.5}O_{19}$	0.1641	0.07565	4.3933	0.1774	2.5832
$Sr_{0.82}Sm_{0.18}Fe_{11}Al_1O_{19}$	0.1663	0.07669	4.2605	0.3596	2.6189
$Sr_{0.82}Sm_{0.18}Fe_{10.5}Al_{1.5}O_{19}$	0.1687	0.07777	4.1238	0.5471	2.6557
$Sr_{0.82}Sm_{0.18}Fe_{10}Al_2O_{19}$	0.1712	0.07896	3.9874	0.7405	2.6963
Gd doped Samples	$Sr(NO_3)_2$	$Gd(NO_3)_3{\cdot}6H_2O$	$Fe(NO_3)_3{\cdot}9H_2O$	$Al(NO_3)_3{\cdot}9H_2O$	Citric Acid
$Sr_{0.82}Gd_{0.18}Fe_{12}O_{19}$	0.1615	0.07562	4.5124	0.000	2.5427
$Sr_{0.82}Gd_{0.18}Fe_{11.5}Al_{0.5}O_{19}$	0.1637	0.07655	4.3833	0.1769	2.5773
$Sr_{0.82}Gd_{0.18}Fe_{11}Al_1O_{19}$	0.1659	0.07771	4.2506	0.3588	2.6129
$Sr_{0.82}Gd_{0.18}Fe_{10.5}Al_{1.5}O_{19}$	0.1683	0.07879	4.1142	0.5457	2.6495
$Sr_{0.82}Gd_{0.18}Fe_{10}Al_2O_{19}$	0.1707	0.07991	3.9739	0.7379	2.6872

The balanced chemical reaction during the process is given as:

$$0.82\mathrm{Sr}(\mathrm{NO}_3)_2 + 0.18\mathrm{RE}(\mathrm{NO}_3)_3 + (12-x)\mathrm{Fe}(\mathrm{NO}_3)_3 + x\mathrm{Al}(\mathrm{NO}_3)_3 + \mathrm{C}_6\mathrm{H}_8\mathrm{O}_7 + \mathrm{NH}_4\mathrm{OH} \rightarrow \mathrm{Sr}_{0.82}\mathrm{RE}_{0.18}\mathrm{Fe}_{12-x}\mathrm{Al}_x\mathrm{O}_{19} + \mathrm{NH}_4\mathrm{NO}_3 + \mathrm{CO}_2 + \mathrm{H}_2\mathrm{O} \quad (1)$$

The crystal phases of the synthesized powders were determined by X-ray diffraction (XRD, Bruker D8 Advance, Germany) using Cu *Ka* (λ = 1.5406 Å) as the radiation source (40 kV, step size 0.02, scan rate 0.2 min/step, 20˚ ≤ 2θ ≤ 70˚). FTIR spectra were collected in transmission geometry on a disc-shaped sample prepared by mixing KBr 95 Wt% with samples of 5 Wt%. Thermo Nicolet iS 10 was used to collect FTIR spectra. Room temperature magnetic parameters were obtained from demagnetization curves measured using SQUID (Quantum Design, Inc.) with the sweeping magnetic field ± 50 KOe. A 6 mm diameter and 2 mm thick disc were prepared by mixing the powder with PVA Wt% in 200 mg powder samples. The pressure of 5 MPa was applied on samples using a press die. Electric measurement, including resistivity, was performed on the disc-shaped samples in a temperature range up to 190˚C using two probe method (TPR-EXP, SVS Labs, CA, USA). The activation energy was measured using the Arrhenius equation [25] is given by

$$\rho = \rho_0 \exp\left(\frac{E_a}{K_B T}\right) \quad (2)$$

where E_a is the activation energy and K_B is the Boltzmann constant. The activation energy in the present case was obtained by fitting the DC resistivity data. Dielectric measurements were performed on the same sample in the low-frequency range from 10 kHz to 10 MHz using HP 4275A Multi-Frequency LCR Meter and high-frequency range from 200 MHz to 13,700 MHz using Field Fox Analyzer (N9915A).

3. Result and Discussion

The room temperature XRD pattern of $Sr_{0.82}RE_{0.18}Fe_{12-x}Al_xO_{19}$ is shown in **Figures 1(a)-(c)**. It is found from the diffraction pattern that samples are single-phase magnetoplumbite structure (ICCD 080-1198) with small additional secondary phase Fe_2O_3. The phase of the as-prepared ferrite corresponds to the hexagonal $P6_3/mmc$ symmetry group. The inset of **Figure 1** gives the expanded view of the diffracted peaks (107), (200) and (203) between 2θ = 34˚ - 38˚. The peaks are shifting towards higher 2θ values implying the contraction of the lattice with Al^{3+} substitution. Observed peak broadening with Al^{3+} content also indicate a decrease in crystallite size of the $Sr_{0.82}RE_{0.18}Fe_{12-x}Al_xO_{19}$. Furthermore, the presence of secondary phase $Fe_2O_3$was observed to increase with the atomic weight of the rare-earth viz., Pr^{3+}, Sm^{3+}, Gd^{3+}. Additional, secondary phases, such as $Gd(FeO_3)$, $PrFe_2O_3$, and $SmFe_2O_3$ were also observed. The secondary phase obtained in Pr^{3+} doped samples is found to be smaller as compared to Sm^{3+} and Gd^{3+} doped samples.

The XRD data of all three sets of the sample was fitted and analyzed using

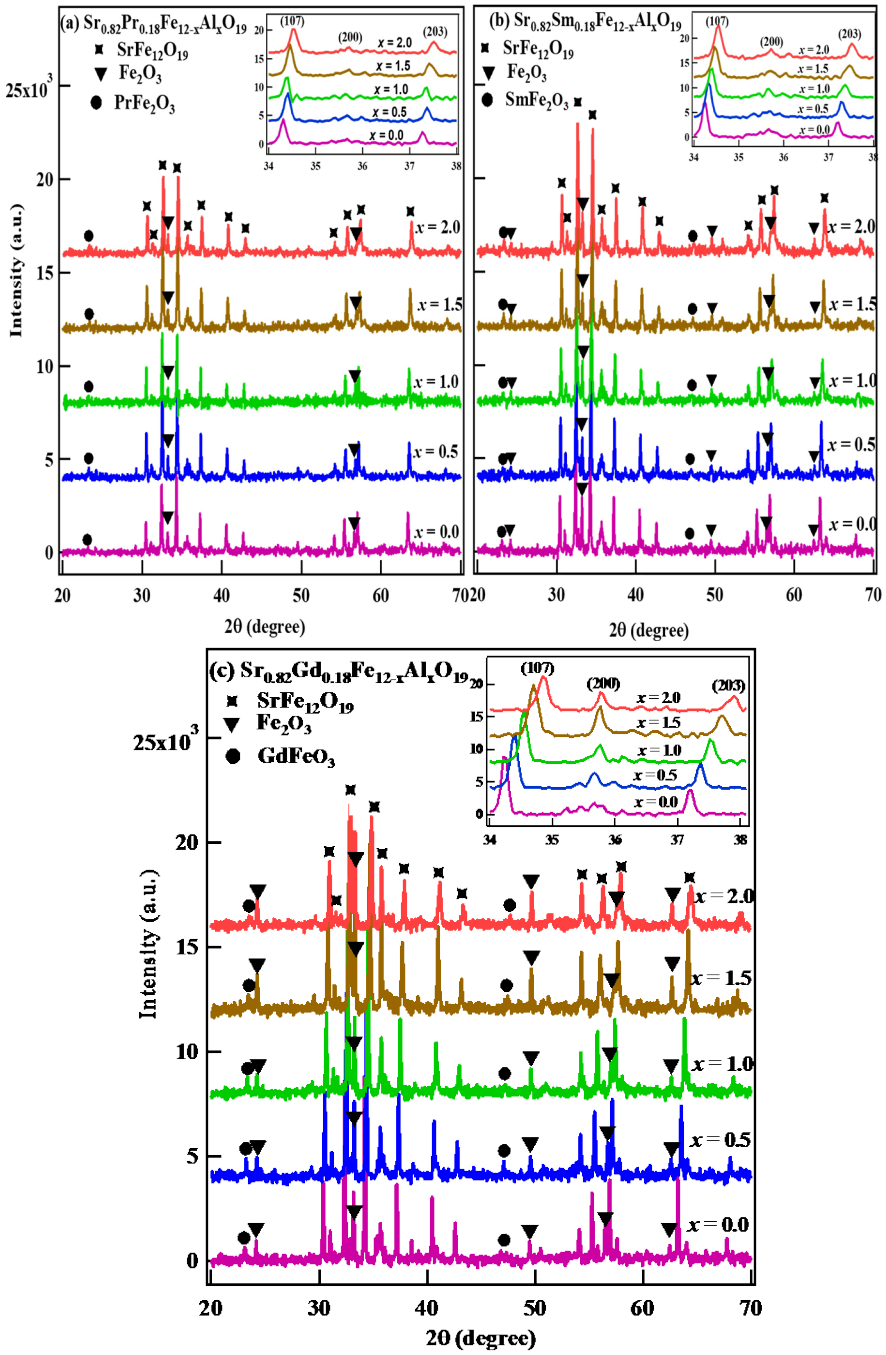

Figure 1. XRD patterns of (a) $Sr_{0.82}Pr_{0.18}Fe_{12-x}Al_xO_{19}$ (b) $Sr_{0.82}Sm_{0.18}Fe_{12-x}Al_xO_{19}$ $Sr_{0.82}$ (x = 0.0, 0.5, 1.0, 1.5, 2.0). XRD patterns of (c) $Sr_{0.82}Gd_{0.18}Fe_{12-x}Al_xO_{19}$ (x = 0.0, 0.5, 1.0, 1.5, 2.0).

TOPAS software to determine the lattice parameters "*a*", "*c*" and the unit cell volume, "*V*" of $Sr_{0.82}RE_{0.18}Fe_{12-x}Al_xO_{19}$. Lattice parameters of $Sr_{0.8}RE_{0.18}Fe_{12-x}Al_xO_{19}$ are listed in Table 2 and plotted as a function of RE^{3+} and Al^{3+} content in Figures 2(a)-(c). It is observed from Figures 2(a)-(c) that "*a*" and "*c*" and "*V*" decrease at a rate of −0.0238 Å, −0.0979 Å and −8.33 Å^3 per Al^{3+} content, respectively with increasing Al^{3+} substitution. The decrease in lattice parameters "*a*" and "*c*," and the unit cell volume, "*V*," is due to smaller radii of Al^{3+} (0.535 Å)

Table 2. Lattice parameters "*a*", "*c*" and "*V*" and crystallite size of $Sr_{0.82}RE_{0.18}Fe_{12-x}Al_xO_{19}$.

Samples	*a* (Å)	*c* (Å)	*V* (Å^3)	Crystallite size (HWL) nm	Micro deformation (-ε)
$Sr_{0.82}Pr_{0.18}Fe_{12}O_{19}$	5.88563	23.0744	692.224	47.8	0.0049
$Sr_{0.82}Pr_{0.18}Fe_{11.5}Al_{0.5}O_{19}$	5.86557	22.9962	685.183	45.7	0.0049
$Sr_{0.82}Pr_{0.18}Fe_{11}Al_1O_{19}$	5.85534	22.9462	680.397	44.0	0.0051
$Sr_{0.82}Pr_{0.18}Fe_{10.5}Al_{1.5}O_{19}$	5.84753	22.9147	678.562	42.9	0.005
$Sr_{0.82}Pr_{0.18}Fe_{10}Al_2O_{19}$	5.83511	22.8703	674.699	40.8	0.0054
$Sr_{0.82}Sm_{0.18}Fe_{12}O_{19}$	5.87716	23.0498	689.493	49.4	0.0042
$Sr_{0.82}Sm_{0.18}Fe_{11.5}Al_{0.5}O_{19}$	5.86394	22.9882	684.475	44.9	0.0052
$Sr_{0.82}Sm_{0.18}Fe_{11}Al_1O_{19}$	5.85402	22.9404	678.345	42.7	0.005
$Sr_{0.82}Sm_{0.18}Fe_{10.5}Al_{1.5}O_{19}$	5.84225	22.8972	676.823	41.7	0.005
$Sr_{0.82}Sm_{0.18}Fe_{10}Al_2O_{19}$	5.83245	22.8635	673.558	40.1	0.0055
$Sr_{0.82}Gd_{0.18}Fe_{12}O_{19}$	5.87874	23.0475	688.891	46.3	0.0042
$Sr_{0.82}Gd_{0.18}Fe_{11.5}Al_{0.5}O_{19}$	5.86246	22.9741	683.799	42.1	0.0052
$Sr_{0.82}Gd_{0.18}Fe_{11}Al_1O_{19}$	5.84994	22.9343	676.984	40.5	0.0048
$Sr_{0.82}Gd_{0.18}Fe_{10.5}Al_{1.5}O_{19}$	5.83809	22.8907	674.356	39.7	0.0057
$Sr_{0.82}Gd_{0.18}Fe_{10}Al_2O_{19}$	5.83107	22.8607	673.157	38.6	0.0059

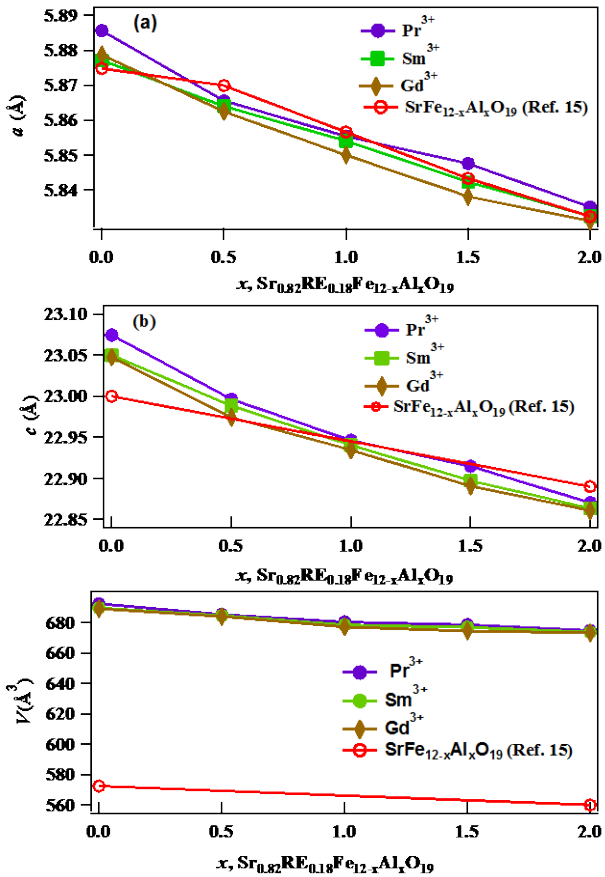

Figure 2. Lattice parameter as (a) "*a*" and (b) "*c*" (c) volume "*V*" of $Sr_{0.82}RE_{0.18}Fe_{12-x}Al_xO_{19}$ as a function of Al^{3+} content (RE^{3+} = Pr^{3+}, Sm^{3+}, Gd^{3+}, x = 0.0, 0.5, 1.0, 1.5, 2.0).

replacing Fe^{3+} (0.65 Å) [24]. It is evident from **Table 2** that overall Pr^{3+}-Al^{3+} substituted samples display higher lattice parameter values as compared to other RE^{3+} (Sm^{3+}, Gd^{3+}) doped $Sr_{0.82}RE_{0.18}Fe_{12-x}Al_xO_{19}$. The higher lattice parameter value of Pr^{3+} doped sample results from its bigger ionic radii (1.13 Å) as compared to the radii of Sm^{3+} (1.098 Å) and Gd^{3+} (1.078 Å) upon replacing Sr^{2+} (1.38 Å) [24].

The average crystallite size and micro-deformation were determined by using Halder-Wagner-Langford's (HWL) plot technique applied to the XRD data [26]. According to HWL, the relationship between FWHM of x-ray diffraction peaks, "β", with the mean crystallize size, "T", and the micro-deformation of a grain, "ε", is given

$$\left(\frac{\beta^*}{d^*}\right)^2 = \frac{1}{T}\left(\frac{\beta^*}{d^{*2}}\right) + \left(\frac{\varepsilon}{2}\right)^2 \tag{3}$$

where β^* is given by $\beta^* = \frac{\beta}{\lambda}\cos(\theta)$, λ the x-rays wavelength, and d^* is given as $d^* = \frac{2}{\lambda}\sin(\theta)$. The plot of the Equation (3) is shown in **Figures 3(a)-(c)**.

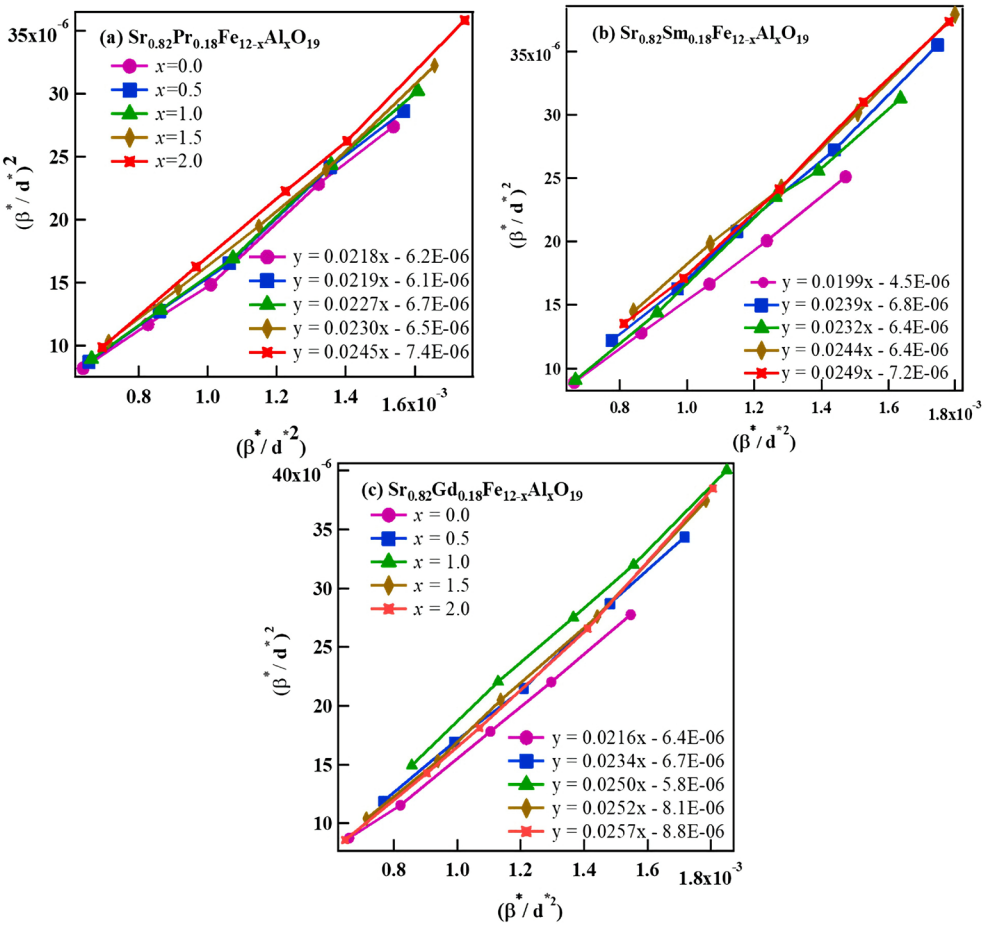

Figure 3. Halder-Wagner-Langford"s (HWL) plot of (a) $Sr_{0.82}Pr_{0.18}Fe_{12-x}Al_xO_{19}$, (b) $Sr_{0.82}Pr_{0.18}Fe_{12-x}Al_xO_{19}$, and (c) $Sr_{0.82}Gd_{0.18}Fe_{12-x}Al_xO_{19}$ (x = 0.0, 0.5, 1.0, 1.5, 2.0).

Crystallite size and micro-strain deformation measured from the plot is summarized in Table 2. The variation of the crystallite size of $Sr_{0.82}Pr_{0.18}Fe_{12-x}Al_xO_{19}$ as a function of Al^{3+} content is shown in Figure 4. The decrease in the crystallite size is because RE^{3+}-Al^{3+} substitution inhibits the grain growth as they enter into grain boundaries and accelerate the formation of secondary phases. The observed secondary phases cause the grain refinement accompanied by reduced strain [27].

The mean crystallite size of $Sr_{0.82}RE_{0.18}Fe_{12-x}Al_x$ calculated using Halder-Wagner Langford's (HWL) plot technique follows a decreasing trend with increasing Al^{3+} content. The measured mean crystallite size of $Sr_{0.82}Pr_{0.18}Fe_{12-x}Al_xO_{19}$ (47.8 to 40.8 nm), $Sr_{0.82}Sm_{0.18}Fe_{12-x}Al_xO_{19}$ (49.4 to 40.1 nm) and $Sr_{0.82}Gd_{0.18}Fe_{12-x}Al_xO_{19}$ (46.3 to 38.6 nm) for $x = 0.0$ to $x = 2.0$. It has been observed that the value of crystallite size is highest for Pr^{3+} and lowest for Gd^{3+} doped samples in agreement with their ionic radii *i.e.* Pr^{3+} (1.13 Å) > Sm^{3+} (1.098 Å) > Gd^{3+} (1.078 Å).

Overall observed strain in Gd^{3+} doped $Sr_{0.82}Gd_{0.18}Fe_{12-x}Al_xO_{19}$ is higher than other RE^{3+} (Pr^{3+}, Sm^{3+}) doped samples. The higher value of strain in Gd^{3+} (with spherical 4*f* charge distribution) doped samples is due to its smaller radii, which may result in the secondary phases as confirmed via XRD [28] [42]. It has been reported earlier by Lechiviller *et al.* [29] that Pr^{3+}, with oblate 4*f* charge distribution, is easily accommodated in $SrFe_{12}O_{19}$ unit cell. Thus, our results confirm the fact that the 4*f* charge symmetry of rare-earth controls the accommodation of RE^{3+} in $SrFe_{12}O_{19}$ unit cell. Sm^{3+} (positive Stevens constant, α_J) and Gd^{3+} (zero Stevens constant) are thus not as desired as Pr^{3+} (negative Stevens constant), as the later produces minimum lattice distortion and secondary phases [30].

FTIR spectra of $Sr_{0.82}RE_{0.18}Fe_{12-x}Al_xO_{19}$ is shown in Figure 5. From Figure 5,

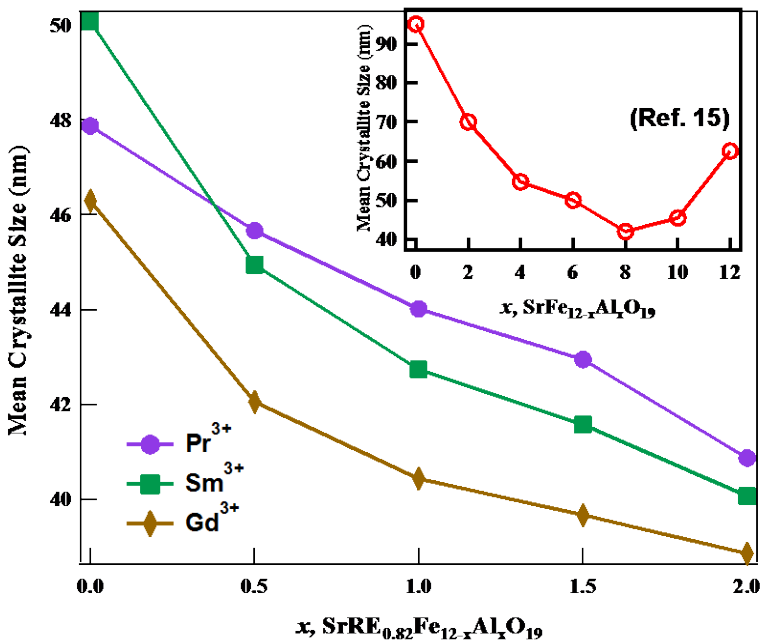

Figure 4. Variation of mean crystallite size of $Sr_{0.82}RE_{0.18}Fe_{12-x}Al_xO_{19}$ as a function of Al^{3+} content (RE^{3+} = Pr^{3+}, Sm^{3+}, Gd^{3+}, $x = 0.0, 0.5, 1.0, 1.5, 2.0$).

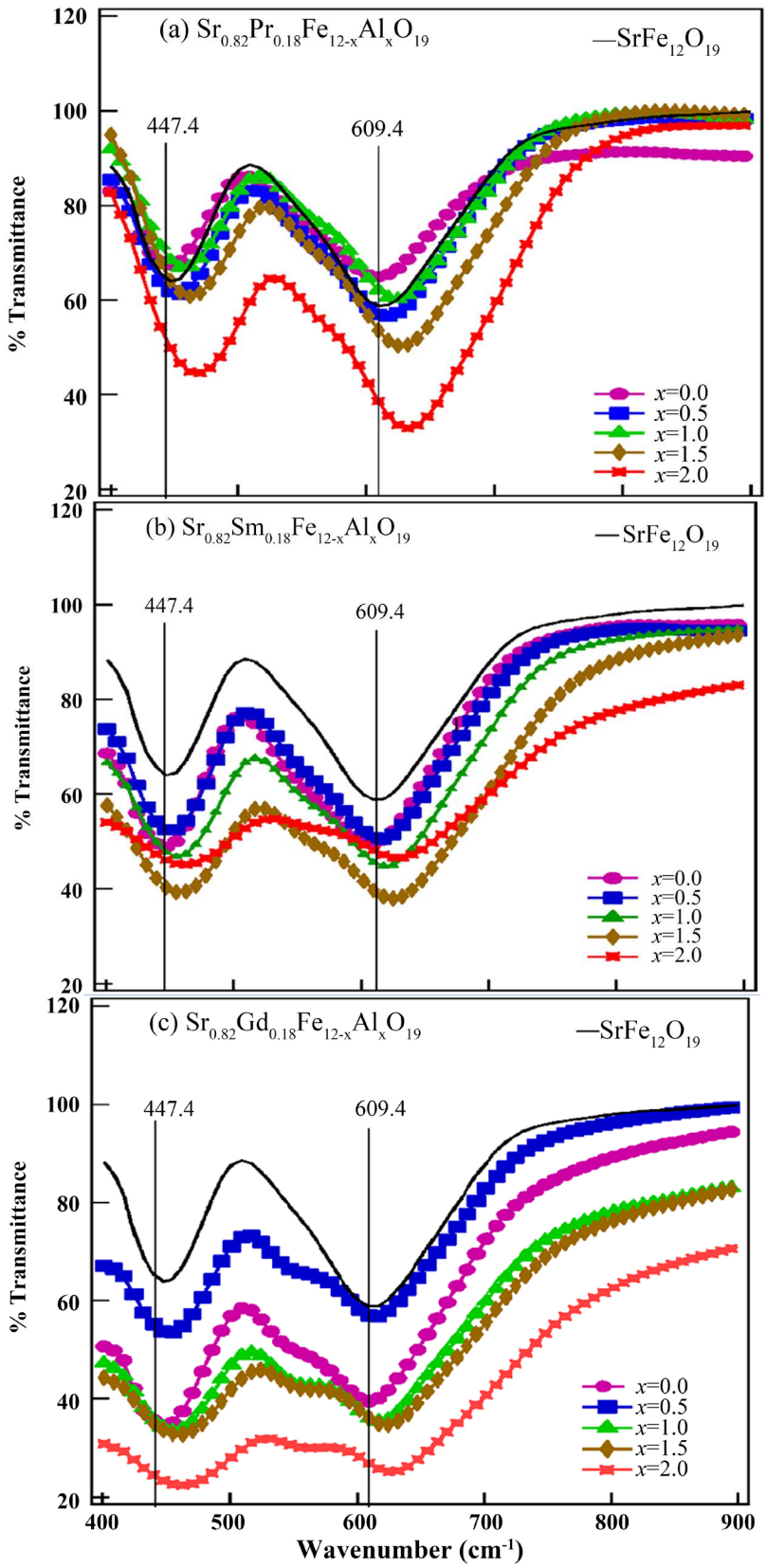

Figure 5. FTIR spectra of (a) $Sr_{0.82}Pr_{0.18}Fe_{12-x}Al_xO_{19}$, (b) $Sr_{0.82}Sm_{0.18}Fe_{12-x}Al_xO_{19}$, and (c) $Sr_{0.82}Gd_{0.18}Fe_{12-x}Al_xO_{19}$.

the FTIR spectrum of $Sr_{0.82}RE_{0.18}Fe_{12-x}Al_xO_{19}$ exhibit two high-frequency bands in the range between 900 cm^{-1} to 400 cm^{-1}. The frequency absorption bands at 609.4 cm^{-1}, and 447.4 cm^{-1} corresponds to tetrahedral and octahedral M-O stretching vibration of the pure Sr-ferrite, respectively. These absorption bands correspond to the typical absorption of $SrFe_{12}O_{19}$ [31] [32] [33]. A very approximate bands were also observed in the $SrZr_{0.2}Cd_{0.2}Fe_{11.6}O_{19}$ [18]. The shifting of absorption bands towards higher frequency has been observed with increasing Al^{3+} content. This shift in the wavenumber is due to higher energy absorption accompanied by a change in bond-length. **Table 3** shows the wavenumber of the corresponding absorption peaks of $Sr_{0.82}RE_{0.18}Fe_{12-x}Al_xO_{19}$. As the wavenumber shift is inversely proportional to the atomic mass, substitution for heavier Fe^{3+} by lighter Al^{3+} will thus lead to an increase in wavenumbers [27]. This shift in wavenumber to the higher values with increasing Al^{3+} content could also result from the decrease in bond length between Fe^{3+}-O^{2-} in the B-sites with the lattice contraction. The higher wavenumber shift is observed in Pr^{3+} doped samples as compared to other RE^{3+} (Sm^{3+}, Gd^{3+}) doping in $Sr_{0.82}RE_{0.18}Fe_{12-x}Al_xO_{19}$. Even though Pr^{3+} doped $Sr_{0.82}RE_{0.18}Fe_{12-x}Al_xO_{19}$ has a higher lattice volume, the shift in wavenumber to high values suggest tight bonding with near neighbor O^{2-}. This again indicates that RE^{3+} with negative α_j (Pr^{3+}) can fit well into $Sr_{0.82}RE_{0.18}Fe_{12-x}Al_xO_{19}$ unit cell. Also, Pr^{3+} is lighter than Sm^{3+} and Gd^{3+}, thus Pr^{3+}-Al^{3+} display slightly greater shift in wavenumber than Sm^{3+}-Al^{3+} and Gd^{3+}-Al^{3+} doped samples [34]. The vibrations bands are broadened by the substitution of RE^{3+} ions shown in **Figures 5(a)-(c)** is due to the decrease in particle size with doping ions [35].

Figure 6 shows RT demagnetization curves $Sr_{0.82}RE_{0.18}Fe_{12-x}Al_xO_{19}$ obtained using SQUID. The magnetic parameters saturation magnetization, remanence, and coercivity were extracted from the demagnetization curves and are listed in **Table 4**. The demagnetization curves show the characteristic behavior of hard ferrites with high coercivity. The saturation magnetization, M_s of $Sr_{0.82}RE_{0.18}Fe_{12-x}Al_xO_{19}$ as a function of Al^{3+} content, is plotted in **Figure 7**. The magnetic properties of the substituted ferrite in comparison to pure $SrFe_{12}O_{19}$ has been changed significantly upon RE^{3+} and Al^{3+} substitution in $Sr_{0.82}RE_{0.18}Fe_{12-x}Al_xO_{19}$. On an average

Table 3. Wave numbers for peak 1 and peak 2 of $Sr_{0.82}RE_{0.18}Fe_{12-x}Al_xO_{19}$ obtained from FTIR measurements.

Al^{3+} content,	Wave-number(cm^{-1})		Wave-number (cm^{-1})		Wave-number (cm^{-1})	
x	for Pr^{3+}-Al^{3+} samples		for Sm^{3+}-Al^{3+}-doped samples		for Gd^{3+}-Al^{3+}-doped samples	
	Peak 1	Peak 2	Peak 1	Peak 2	Peak 1	Peak 2
0.0	447.40	609.40	447.40	609.4	447.40	609.40
0.5	455.12	617.11	455.12	617.11	445.12	617.11
1.0	462.83	624.82	455.12	617.11	455.12	617.11
1.5	462.83	624.82	455.12	624.82	462.83	624.82
2.0	470.55	632.54	462.83	624.82	462.83	624.82

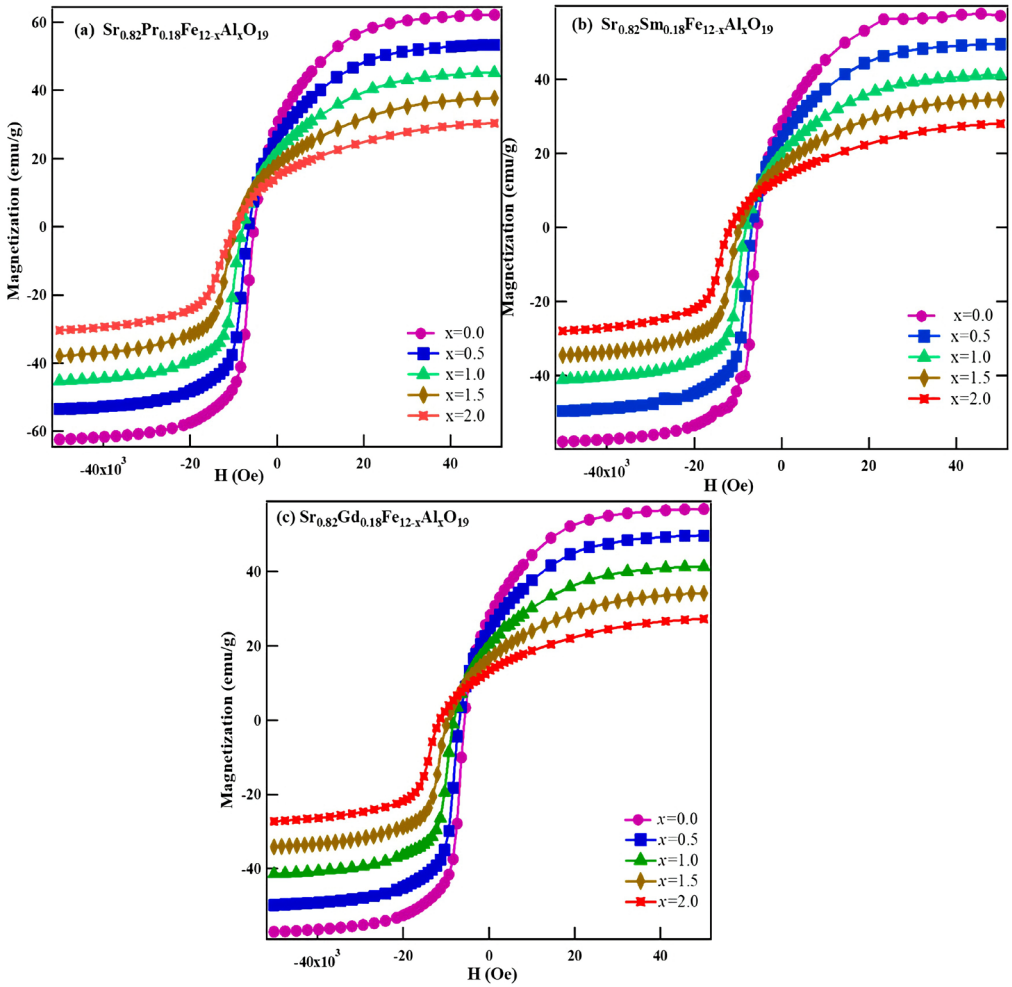

Figure 6. Room temperature demagnetization curves of (a) $Sr_{0.82}Pr_{0.18}Fe_{12-x}Al_xO_{19}$ (b) $Sr_{0.82}Sm_{0.18}Fe_{12-x}Al_xO_{19}$ (c) $Sr_{0.82}Gd_{0.18}Fe_{12-x}Al_xO_{19}$.

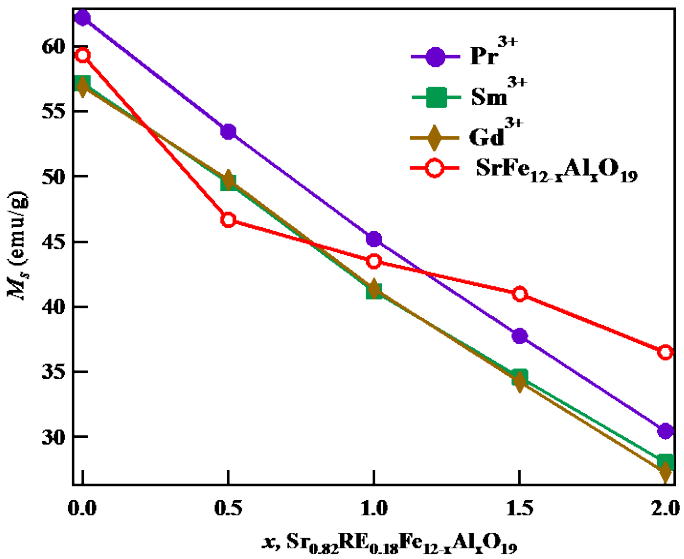

Figure 7. Variation of saturation magnetization, M_s, of $Sr_{0.82}RE_{0.18}Fe_{12-x}Al_xO_{19}$ as a function of Al^{3+} content (RE^{3+} = Pr^{3+}, Sm^{3+}, Gd^{3+}, x = 0.0, 0.5, 1.0, 1.5, 2.0).

Table 4. Resistivity ($\times 10^7$ Ω-cm) of $Sr_{0.82}RE_{0.18}Fe_{12-x}Al_xO_{19}$ (RE^{3+} = Pr^{3+}, Sm^{3+}, Gd^{3+}, x = 0.0, 0.5, 1.0, 1.5, 2.0).

Composition	$x = 0.0$	$x = 0.5$	$x = 1.0$	$x = 1.5$	$x = 2.0$
$Sr_{0.82}Pr_{0.18}Fe_{12-x}Al_xO_{19}$	0.1498	0.1828	0.1983	1.1940	1.286
$Sr_{0.82}Sm_{0.18}Fe_{12-x}Al_xO_{19}$	0.1262	0.1521	0.7061	0.9106	1.145
$Sr_{0.82}Gd_{0.18}Fe_{12-x}Al_xO_{19}$	1.0580	10.222	10.920	10.223	15.24

the saturation magnetization, M_s decreases linearly with Al^{3+} content at the rate of −15.8 emu/g per Al^{3+} substitution.

The M_s value is maximum for Pr^{3+}-Al^{3+} doped ferrite (62.24 emu/g) and minimum for Gd^{3+} doped ferrite (56.88 emu/g) for (x = 0). This variation of magnetic properties can be explained based on the site occupancy of the substituted ions. The magnetic moment in M-type hexaferrite is due to the distribution of iron on five non-equivalent sublattices of which three are octahedral (2a, 12*k*, and 4*f*2), one tetrahedral (4*f*1) and one trigonal bipyramidal (2*b*) [4]. The sites 12*k*, 2a, and 2b have upward spins, and 4*f*1 and 4*f*2 have a downward spin of electrons. The non-magnetic Al^{3+} ion replaces Fe^{3+} ion (5 μ_B) from the sites having spin up direction, mainly 12*k*, which is responsible for the reduction in saturation magnetization and remanence of the synthesized materials [15] [36] [37].

The decrease in magnetization is also attributed to the lattice contraction with the substitution of RE^{3+} and Al^{3+}, which changes the bond angle of Fe^{3+}-O^{2-}-Fe^{3+} and alters the strength of the super-exchange interaction. To maintain the charge neutrality, the substitution of Sr^{2+} with RE^{3+} also changes some Fe^{3+} to Fe^{2+} and thus further reduces the net magnetic moment per unit volume, causing the decrease in magnetization. The magnetization also decreases due to the increased amount of paramagnetic secondary phases in heavier RE^{3+} doped $Sr_{0.82}RE_{0.18}Fe_{12-x}Al_xO_{19}$ samples.

The variation of M_r/M_s of $Sr_{0.82}RE_{0.18}Fe_{12-x}Al_xO_{19}$ as a function of Al^{3+} content is plotted in **Figure 8**. Most of the samples exhibit the squareness ratio of approximately 0.5. This ratio measures the squareness of the hysteresis loop. According to Stoner-Wohlfarth relation [38], a squareness ratio of 0.5 or more indicates that the particles are single magnetic domain while with values much lower than 0.5 indicate the formation of the multidomain structure in the material. The observed M_r/M_s values are very close to 0.5, which indicate the presence of monodomain particles in the sample.

The variation of coercivity of $Sr_{0.82}RE_{0.18}Fe_{12-x}Al_xO_{19}$ as a function of Al^{3+} content is shown in **Figure 9**. The coercivity of samples increases linearly with increasing value of Al^{3+} content. It is observed that the coercivity of the RE^{3+}-Al^{3+} doped samples is significantly higher than that of coercivity of only Al^{3+} doped $SrFe_{12-x}Al_xO_{19}$. The coercivity of $SrFe_{12}O_{19}$ is often associated to the magnetocrystalline anisotropy of trigonal pyramidal 2*b* site [15] [39] [40]. The higher concentration of Al^{3+} doping causes a decrease in a number of Fe^{3+} ions at 2*b*

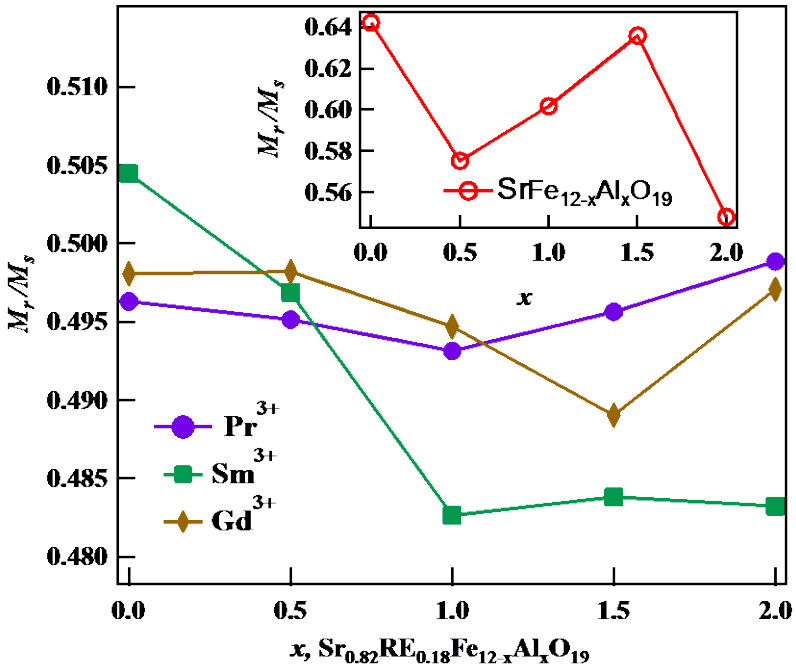

Figure 8. Variation of M_r/M_s of $Sr_{0.82}RE_{0.18}Fe_{12-x}Al_xO_{19}$ as a function of Al^{3+} content (RE^{3+} = Pr^{3+}, Sm^{3+}, Gd^{3+}, x = 0.0, 0.5, 1.0, 1.5, 2.0).

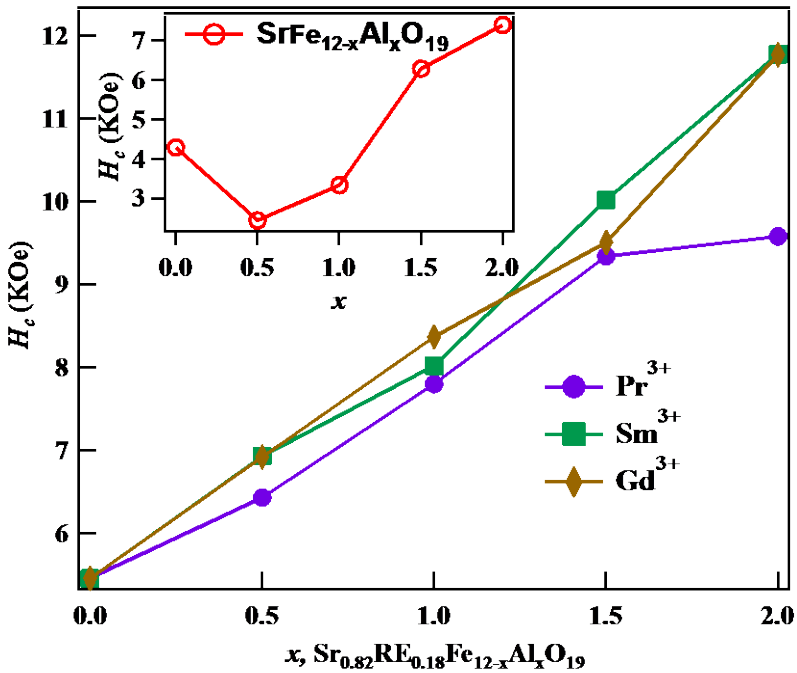

Figure 9. Variation of coercivity, H_c, of $Sr_{0.82}RE_{0.18}Fe_{12-x}Al_xO_{19}$ as a function of Al^{3+} content (RE^{3+} = Pr^{3+}, Sm^{3+}, Gd^{3+}, x = 0.0, 0.5, 1.0, 1.5, 2.0).

sites, which in turn, changes magnetocrystalline anisotropy significantly [15]. In addition, Al^{3+} doping case distortion of 2*b* site, which alters the magnetocrystalline anisotropy of 2*b* site [41]. This collective change in anisotropy promotes an increase in coercivity.

Stoner-Wohlfarth relation [38] shows that $H_c = K_1/M_s$, where K_1 is magnetocrystalline anisotropy, and M_s is saturation magnetization. With Al^{3+} doping, saturation magnetization, M_s decreases thus coercivity, H_c increases. A decrease in saturation magnetization, M_s and changes in K_1, enhance the coercivity of $Sr_{0.82}RE_{0.18}Fe_{12-x}Al_xO_{19}$ with Al^{3+} substitution. The grain size also affects the coercivity since the grain size of Al^{3+} doped sample is smaller the critical size 560 nm of $SrFe_{12}O_{19}$ [4]; the particles in the sample are single domain. In the absence of a domain wall, the energy required to flip the moment is high. Thus, the grain refinement additionally contributes to the coercivity [23]. Among doped samples, Gd^{3+}-Al^{3+} doped samples show high coercivity, most likely due to its finer grain size (**Table 2**) as compared to other RE^{3+} (Pr^{3+}, Sm^{3+})-Al^{3+} doped $Sr_{0.82}RE_{0.18}Fe_{12-x}Al_xO_{19}$ samples.

The variation of Curie temperature, T_c, as a function of Al^{3+} content for $Sr_{0.82}RE_{0.18}Fe_{12-x}Al_xO_{19}$ is shown in **Figure 10**, and values are listed in **Table 4**. From **Figure 10**, it is observed that T_c is decreasing with Al^{3+} content. The T_c decreases at the rate of −58˚C per Al^{3+} content of all the samples. The Pr^{3+} substituted ferrite exhibits a maximum value of T_c ~ 465.21˚C for $x = 0$. The following factors affect the T_c: 1) substitution of Al^{3+} for Fe^{3+} decreases the number and strength of the super-exchange interaction, Fe^{3+}-O^{2-}-Fe^{3+}, 2) conversion of higher spin Fe^{3+} to lower spin Fe^{2+}, to maintain charge neutrality, with RE^{3+} substitution also reduces the strength of super-exchange interaction, and 3) lattice contraction alters the bond length of Fe^{3+}-O^{2-}-Fe^{3+} from its optimum value. The above-combined factors lead to the reduction in T_c with RE^{3+}-Al^{3+} substitution. The observed variation of T_c values among RE^{3+} substituted $Sr_{0.82}RE_{0.18}Fe_{12-x}Al_xO_{19}$ results from subtle difference in exchange interaction ensuing from the variation in the lattice distortion upon inserting rare-earth ions of varying ionic radii.

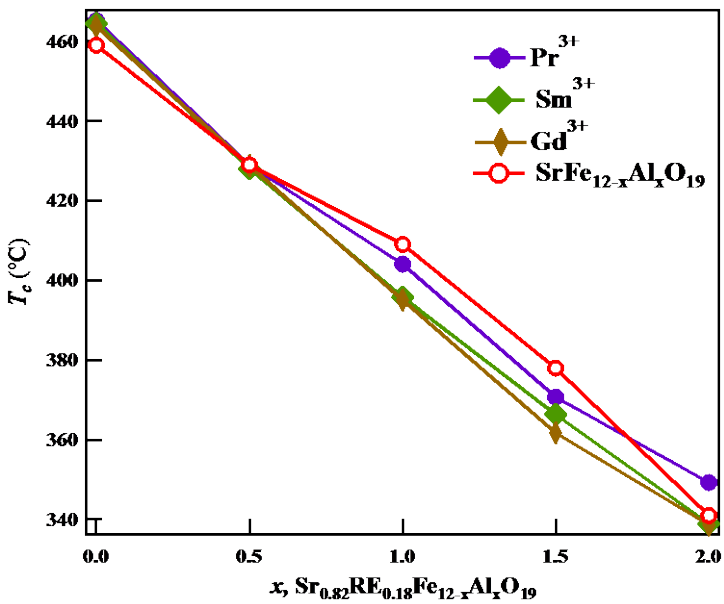

Figure 10. Variation of Cure temperature, T_c, of $Sr_{0.82}RE_{0.18}Fe_{12-x}Al_xO_{19}$ as a function of Al^{3+} content (RE^{3+} = Pr^{3+}, Sm^{3+}, Gd^{3+}, $x = 0.0, 0.5, 1.0, 1.5, 2.0$).

Figures 11(a)-(c) shows the variation of electrical resistivity as function of temperature of $Sr_{0.82}RE_{0.18}Fe_{12-x}Al_xO_{19}$. It is observed that electrical resistivity decreases with temperature exhibiting semiconducting behavior of samples. It is observed that the Al^{3+} doping increases electrical resistivity at room temperature. The highest electrical resistivity was observed for Gd^{3+}-Al^{3+} samples ($\rho \sim 15.2 \times 10^7$ ohm-cm) while the lowest for Pr^{3+}-Al^{3+} sample ($\rho \sim 1.28 \times 10^7$ ohm-cm) for $x = 0.0$. According to Verwey's hopping model, the change in carrier mobility with temperature leads to conduction current by hopping electron between $Fe^{3+} \leftrightarrow Fe^{2+}$ at various sites [42] [43]. The increasing resistivity with Al^{3+} content can be explained based on on-site occupancy, grain size, grain boundaries, etc. As Al^{3+} ion predominantly replaces Fe^{3+} ion at $12k$ octahedral sites, it decreases the number of hopping electrons [17], leading to an increase in electrical resistivity. The number of Fe^{2+} and Fe^{3+} ions is greater in large grain due to which hoping of an electron is easy in the large grain than in smaller grains. Therefore, strontium ferrite with Gd^{3+}-Al^{3+} doped shows higher resistivity.

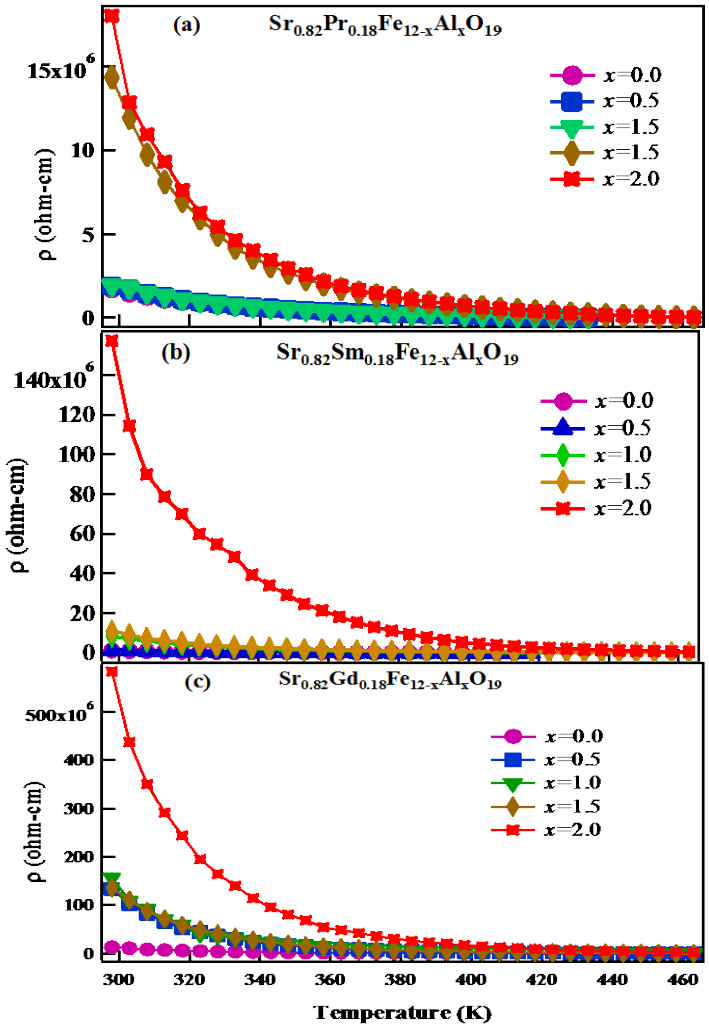

Figure 11. Electrical resistivity as a function of temperature for (a). $Sr_{82}Pr_{0.18}Fe_{12-x}Al_xO_{19}$ (b) $Sr_{0.82}Sm_{0.18}Fe_{12-x}Al_xO_{19}$, and (c) $Sr_{0.82}Gd_{0.18}Fe_{12-x}Al_xO_{19}$.

The activation energy was calculated using the Arrhenius equation by plotting ln(ρ) vs. 1000/T. The ln(ρ) vs. 1000/T plots are shown in Figures 12(a)-(c). The slope of these plots gives activation energy and are listed in Table 5. Figure 13 shows the plot of activation energy vs. RE^{3+}-Al^{3+} content. The activation energy increases with Al^{3+} content in all set of the samples. The activation energy for Gd^{3+}-Al^{3+} doped samples is higher than Sm^{3+}-$Al^{3+}$and Pr^{3+}-Al^{3+} doped samples

Table 5. Activation energy (eV) of $Sr_{0.82}RE_{0.18}Fe_{12-x}Al_xO_{19}$ (RE^{3+} = Pr^{3+}, Sm^{3+}, Gd^{3+}, x = 0.0, 0.5, 1.0, 1.5, 2.0).

Composition	$x = 0$	$x = 0.5$	$x = 1$	$x = 1.5$	$x = 2$
$Sr_{0.82}Pr_{0.18}Fe_{12-x}Al_xO_{19}$	0.2319	0.254	0.2972	0.312	0.3623
$Sr_{0.82}Sm_{0.18}Fe_{12-x}Al_xO_{19}$	0.2692	0.297	0.3271	0.342	0.3875
$Sr_{0.82}Gd_{0.18}Fe_{12-x}Al_xO_{19}$	0.3633	0.4158	0.4283	0.436	0.4532

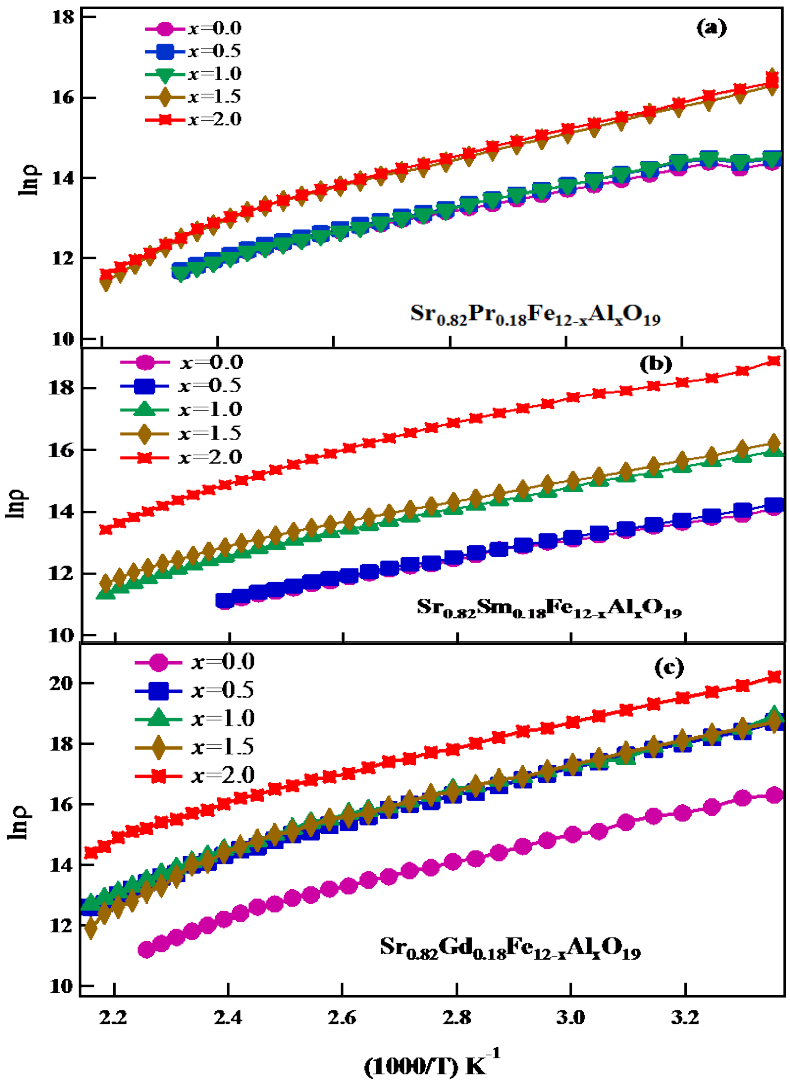

Figure 12. Plot of ln(ρ) as a function of 1000/T for $Sr_{0.82}RE_{0.18}Fe_{12-x}Al_xO_{19}$ (RE^{3+} = Pr^{3+}, Sm^{3+}, Gd^{3+}, x = 0.0, 0.5, 1.0, 1.5, 2.0).

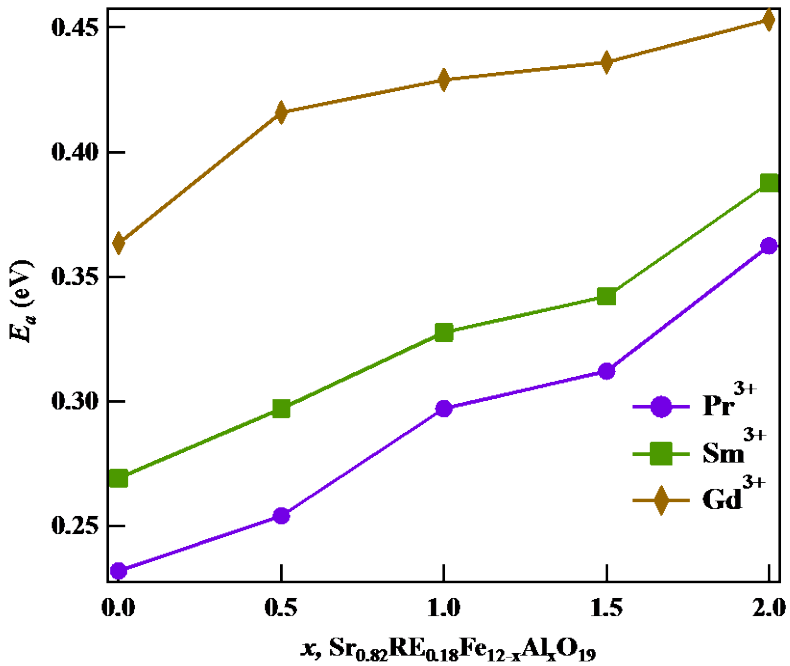

Figure 13. Variation of activation energy of $Sr_{0.82}RE_{0.18}Fe_{12-x}Al_xO_{19}$ as a function of Al^{3+} content ($RE^{3+} = Pr^{3+}, Sm^{3+}, Gd^{3+}$, $x = 0.0, 0.5, 1.0, 1.5, 2.0$).

due to reduced grain size and increased grain boundaries. The activation energy was observed to increase with decreasing ionic radii of RE^{3+} [44]. The increase in activation energy with increasing RE^{3+}-Al^{3+} means that higher energy is required to eject the trapped electron and participate in the conduction mechanism. Also, higher activation energy and enhanced DC resistivity with RE^{3+} substitution are due to the formation of a small amount of additional phases $REFeO_2$ [45].

The variation of dielectric constant and tangent loss (δ) of $Sr_{0.82}RE_{0.18}Fe_{12-x}Al_xO_{19}$ was measured as a function of frequency at room temperature. The dielectric behavior of each sample was found different depending upon types of RE^{3+} and Al^{3+} content. RE^{3+}-Al^{3+} dependence of dielectric constant as function of frequency for $Sr_{0.82}RE_{0.18}Fe_{12-x}Al_xO_{19}$ in low (100 Hz - 10 MHz) and high (200 MHz - 13,700 MHz) frequency range shown in **Figures 14-16**. It is observed that dielectric constant decreases with the increase in frequency in the low-frequency range. However, in the high-frequency range, the dielectric constant initially decreases and becomes constant at above f ≈ 3.5 GHz.

The variation of dielectric constant at frequency shows the dispersion due to Maxwell-Wagner type interfacial polarization [46] associated with Koop's phenomenological theory [47]. Based on these models, the dielectric structure of the ferrite consists of well-conducting grains, separated by highly resistive thin layer grain boundaries formed during the sintering process [22] [48]. At low frequency, there is a large value of dielectric constant due to the grain boundary defects, interfacial dislocation, oxygen vacancies, etc. [49]. At low frequency, applied alternating voltage on the ferrite drops across the thin grain boundaries so that space charge polarization is set up across the grain boundaries. The space charge

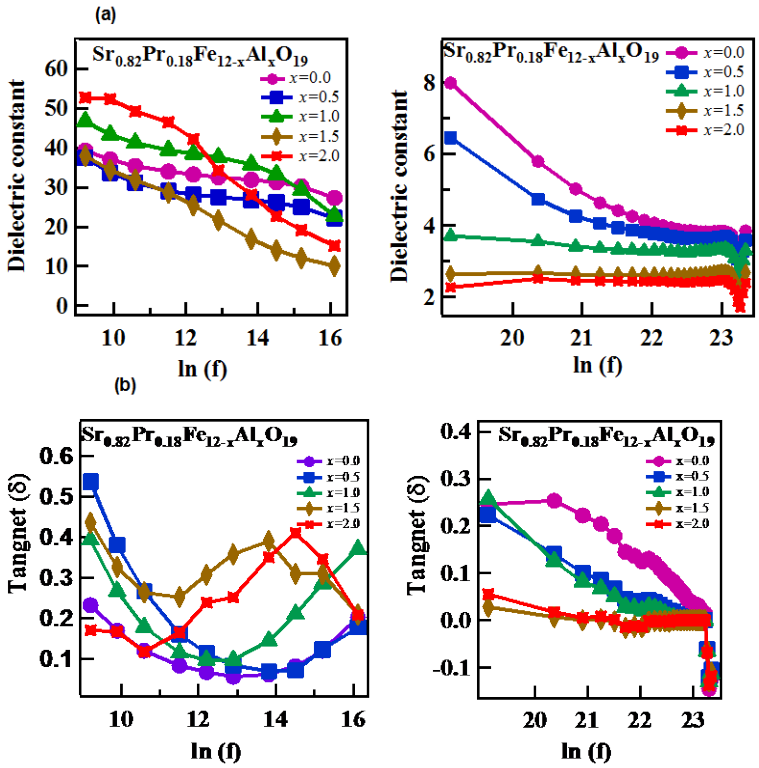

Figure 14. (a) Dielectric Constant and (b) tangent loss of $Sr_{0.82}Pr_{0.18}Fe_{12-x}Al_xO_{19}$ as a function of frequency in low and high frequency range.

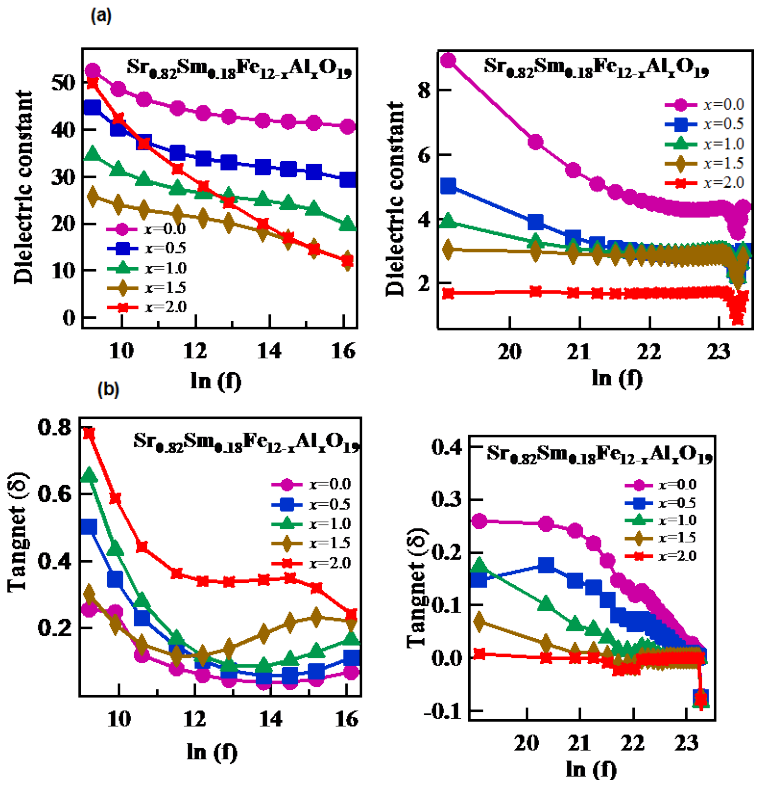

Figure 15. (a) Dielectric Constant and (b) tangent loss of $Sr_{0.82}Sm_{0.18}Fe_{12-x}Al_xO_{19}$ as a function of frequency in low and high frequency range.

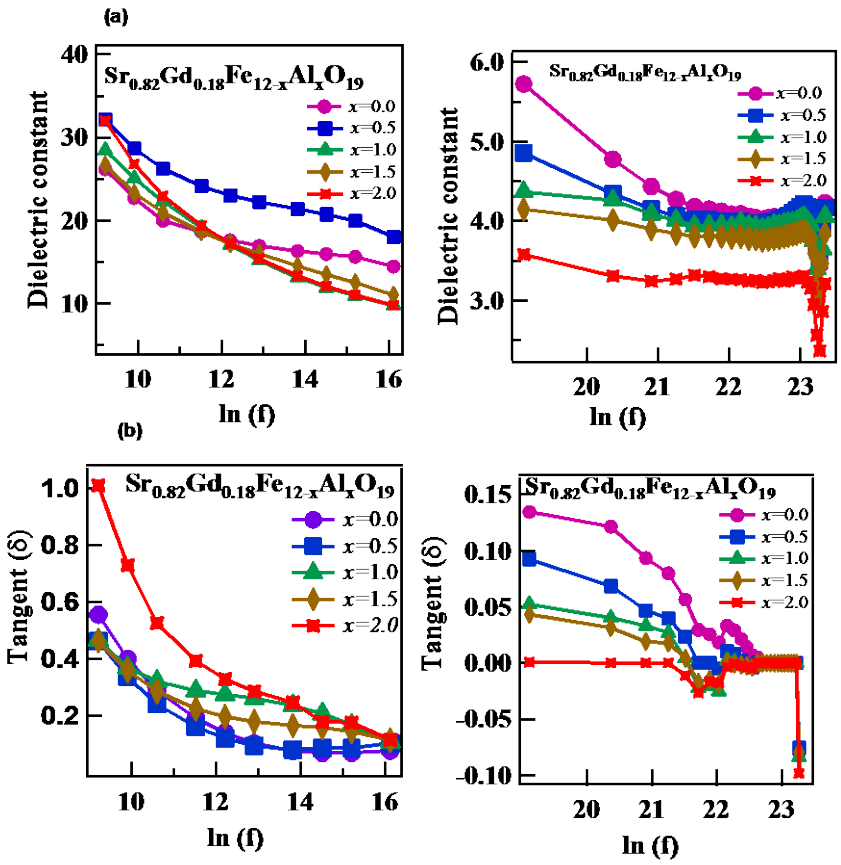

Figure 16. (a) Dielectric Constant and (b) tangent loss of $Sr_{0.82}Gd_{0.18}Fe_{12-x}Al_xO_{19}$ as a function of frequency in low and high frequency range.

polarization is governed by the available free charges on the grain boundaries and conductivity of the sample [50]. For high-frequency range, the dielectric constant decreases with increasing frequency of an external field and become frequency-independent due to the fact that electron hopping between Fe^{2+} and Fe^{3+} cannot follow the alternating field means that frequency of exchange electrons lags behind the frequency of the applied field [36] [43]. The dielectric constant of all set of samples remains almost constant in GHz range, but a sudden drop at ~12.7 GHz is observed due to the fact that the frequency of hopping electron between Fe^{3+} and Fe^{2+} becomes equal to the frequency of the applied alternating field leading to the resonance absorption. The dielectric loss factor decreases with increasing frequency for all sets of samples. The origin of dielectric loss in ferries came from electron hopping in response to low frequency and charged dipole defects response to high frequency [48]. The dielectric loss factor is minimum for Gd^{3+}-Al^{3+} samples, which is attributed to the smallest radial size used among three sets of samples [51].

4. Conclusion

The structural, magnetic, and electrical properties of Re^{3+}-Al^{3+} substitution in $Sr_{0.82}RE_{0.18}Fe_{12-x}Al_xO_{19}$ hexaferrite synthesized via auto-combustion were investi-

gated. The room temperature magnetization was observed to decrease with increase in Al^{3+} substitution in $Sr_{0.82}RE_{0.18}Fe_{12-x}Al_xO_{19}$ due to the magnetic dilution effect, reduction in Fe^{3+}-O^{2-}-Fe^{3+} strength due to lattice contraction, reduction in a number of super-exchange interactions, and conversion of Fe^{3+} to Fe^{2+} with RE^{3+} substitution. The substitution of Al^{3+} for Fe^{3+} was observed to increase the coercivity of $Sr_{0.82}RE_{0.18}Fe_{12-x}Al_xO_{19}$. The increase in coercivity is attributed to a reduction in grain size leading monodomain grains and change in magnetocrystalline anisotropy. A maximum value of 12.21 KOe coercivity was observed for $Sr_{0.82}Gd_{0.18}Fe_{12-x}Al_xO_{19}$ as it also has the smallest grain size among all rare-earth substituted $Sr_{0.82}RE_{0.18}Fe_{12-x}Al_xO_{19}$. Our study suggests that magnetic RE^{3+} enhances coercivity but have a detrimental effect on the saturation magnetization. The oblate charge distribution of Pr^{3+} ions with Stevens's constant $\alpha_j \sim -2.2 \times 10^{-2}$ gets well fitted in the lattice sites, which brings the desired high coercivity. The variation of magnetic properties arises due to the change in magneto-crystalline anisotropy attributed to the site occupancy of RE^{3+} and Al^{3+} ions. The T_c value was observed to decrease with Al^{3+} substitution due to a reduction in super-exchange interactions. The DC electrical resistivity of $Sr_{0.82}RE_{0.18}Fe_{12-x}Al_xO_{19}$ was observed to decrease with increase in temperature. The activation energy was observed to be highest for Gd^{3+} doped $Sr_{0.82}Gd_{0.18}Fe_{12-x}Al_xO_{19}$, which is attributed to increased grain boundaries and reduced grain size. The dielectric constant and dielectric loss were observed to decrease with frequency. This behavior of dielectric constant was attributed to the lagging of hopping electrons behind the applied alternating field. Also, dielectric constant decreases with the Al^{3+} content due to a reduced number of Fe^{3+} ions. As the coercivity and resistivity can be increased without much affecting the magnetization, RE^{3+} substitution in the strontium ferrite is beneficial for microwave devices.

Conflicts of Interest

The authors declare no conflicts of interest regarding the publication of this paper.

References

[1] Shinde, S.R., Lofland, S.E., Ganpule, C.S., Bhagat, S.M., Ogale, S.B., Ramesh, R. and Venkatesan, T. (1999) Improvement in Spin-Wave Resonance Characteristics of Epitaxial Barium-Ferrite Thin Films by Using an Aluminum-Doped Strontium-Ferrite Buffer Layer. *Applied Physics Letters*, **74**, 594-596. https://doi.org/10.1063/1.123156

[2] Dho, J., Lee, E.K., Park, J.Y. and Hur, N. H. (2005) Effects of the Grain Boundary on the Coercivity of Barium Ferrite $BaFe_{12}O_{19}$. *Journal of Magnetism and Magnetic Materials*, **285**, 164-168. https://doi.org/10.1016/j.jmmm.2004.07.033

[3] Jean, M., Nachbaur, V., Bran, J. and Le Breton, J.M. (2010) Synthesis and Characterization of $SrFe_{12}O_{19}$ Powder Obtained by Hydrothermal Process. *Journal of Alloys and Compounds*, **496**, 306-312. https://doi.org/10.1016/j.jallcom.2010.02.002

[4] Zi, Z.F., Sun, Y.P., Zhu, X.B., Yang, Z.R. and Song, W.H. (2008) Structural and Magnetic Properties of $SrFe_{12}O_{19}$ Hexaferrite Synthesized by a Modified Chemical

Co-Precipitation Method. *Journal of Magnetism and Magnetic Materials*, **320**, 2746-2751. https://doi.org/10.1016/j.jmmm.2008.06.009

[5] Guillot, M. and Cahnetal, R.W. (1994) Materials Science and Technology. Wiley-VCH, Weinheim, 1.

[6] Xu, Y., Yang, G.L., Chu, D.P. and Zhai, H.R. (1990) Theory of the Single Ion Magnetocrystalline Anisotropy of 3d Ions. *Physica Status Solidi B*, **157**, 685-693. https://doi.org/10.1002/pssb.2221570221

[7] Liu, X., Zhong, W., Yang, S., Yu, Z., Gu, B. and Du, Y. (2002) Structure and Magnetic Properties of La^{3+} Substituted Strontium Hexaferrite Particles Prepared by Sol-Gel Method. *Physica Status Solidi A*, **193**, 314-319. https://doi.org/10.1002/1521-396X(200209)193:2<314::AID-PSSA314>3.0.CO;2-W

[8] Mocuta, H., Lechevallier, L., Le Breton, J.M., Wang, J.F. and Harris, I.R. (2004) Structural and Magnetic Properties of Hydrothermally Synthesized $Sr_{1-x}Nd_xFe_{12}O_{19}$ Hexagonal Ferrites. *Journal of Alloys and Compounds*, **364**, 48-52. https://doi.org/10.1016/S0925-8388(03)00545-0

[9] Lechevallier, L., Le Breton, J.M., Wang, J.F. and Harris, I.R. (2004) Structural Analysis of Hydrothermally Synthesized $Sr_{1-x}Sm_xFe_{12}O_{19}$ Hexagonal Ferrites. *Journal of Magnetism and Magnetic Materials*, **269**, 192-196. https://doi.org/10.1016/S0304-8853(03)00591-2

[10] Wang, J.F., Ponton, C.B. and Harris, I.R. (2001) A Study of the Magnetic Properties of Hydrothermally Synthesized Sr Hexaferrite with Sm Substitution. *Journal of Magnetism and Magnetic Materials*, **234**, 233-240. https://doi.org/10.1016/S0304-8853(01)00366-3

[11] Wu, Z., Zhang, R., Yu, Z., Shan, L., Dong, L. and Zhang, X. (2018) Study on Preparation and Magnetic Properties of $Sr_{1-x}Gd_xFe_{12-x}Cu_xO_{19}$ ($0.00 \leq x \leq 0.20$) Strontium Ferrite Prepared by Solid Phase Method. *Ferroelectrics*, **523**, 82-88. https://doi.org/10.1080/00150193.2018.1391569

[12] Le Breton, J.M., Teillet, J., Wiesinger, G., Morel, A., Kools, F. and Tenaud, P. (2002) Mossbauer Investigation of Sr-Fe-O Hexaferrites with La-Co Addition. *IEEE Transactions on Magnetics*, **38**, 2952-2954. https://doi.org/10.1109/TMAG.2002.803177

[13] Dahal, J.N., Wang, L., Mishra, S.R., Nguyen, V.V. and Liu, J.P. (2014) Synthesis and Magnetic Properties of $SrFe_{12-x-y}Al_xCo_yO_{19}$ Nanocomposites Prepared via Autocombustion Technique. *Journal of Alloys and Compounds*, **595**, 213-220. https://doi.org/10.1016/j.jallcom.2013.12.186

[14] Nourbakhsh, A.A., Noorbakhsh, M., Nourbakhsh, M., Shaygan, M. and Mackenzie, K.J. (2011) The Effect of Nano Sized $SrFe_{12}O_{19}$ Additions on the Magnetic Properties of Chromium-Doped Strontium-Hexaferrite Ceramics. *Journal of Materials Science: Materials in Electronics*, **22**, 1297-1302. https://doi.org/10.1007/s10854-011-0303-3

[15] Luo, H., Rai, B.K., Mishra, S.R., Nguyen, V.V. and Liu, J.P. (2012) Physical and Magnetic Properties of Highly Aluminum Doped Strontium Ferrite Nanoparticles Prepared by Auto-Combustion Route. *Journal of Magnetism and Magnetic Materials*, **324**, 2602-2608. https://doi.org/10.1016/j.jmmm.2012.02.106

[16] Miller, A. (1959) Distribution of Cations in Spinels. *Journal of Applied Physics*, **30**, S24-S25. https://doi.org/10.1063/1.2185913

[17] Iqbal, M.J., Ashiq, M.N., Hernandez-Gomez, P. and Munoz, J.M. (2008) Synthesis, Physical, Magnetic and Electrical Properties of Al-Ga Substituted Co-Precipitated Nanocrystalline Strontium Hexaferrite. *Journal of Magnetism and Magnetic Materials*, **320**, 881-886. https://doi.org/10.1016/j.jmmm.2007.09.005

[18] Albanese, G., Carbucicchio, M. and Deriu, A. (1974) Temperature Dependence of the Sublattice Magnetizations in Al-and Ga-Substituted M-Type Hexagonal Ferrites. *Physica Status Solidi A*, **23**, 351-358. https://doi.org/10.1002/pssa.2210230202

[19] Ashiq, M.N., Iqbal, M.J. and Gul, I.H. (2009) Structural, Magnetic and Dielectric Propertie of Zr-Cd Substituted Strontium Hexaferrite ($SrFe_{12}O_{19}$) Nanoparticles. *Journal of Alloys and Compounds*, **487**, 341-345. https://doi.org/10.1016/j.jallcom.2009.07.140

[20] Polyko, D.D., Bashkirov, L.A., Trukhanov, S.V., Lobanovskii, L.S. and Sirota, I.M. (2011) Crystal Structure and Magnetic Properties of High-Coercivity $Sr_{1-x}Pr_xFe_{12-x}Zn_xO_{19}$ Solid Solutions. *Inorganic Materials*, **47**, 75-79. https://doi.org/10.1134/S0020168511010110

[21] Qiao, L., You, L., Zheng, J., Jiang, L. and Sheng, J. (2007) The Magnetic Properties of Strontium Hexaferrites with La-Cu Substitution Prepared by SHS Method. *Journal of Magnetism and Magnetic Materials*, **318**, 74-78. https://doi.org/10.1016/j.jmmm.2007.04.028

[22] Corral-Huacuz, J.C. and Mendoza-Suarez, G. (2002) Preparation and Magnetic Properties of Ir-Co and La-Zn Substituted Barium Ferrite Powders Obtained by Sol-Gel. *Journal of Magnetis and Magnetic Materials*, **242**, 430-433. https://doi.org/10.1016/S0304-8853(01)01141-6

[23] Rai, B.K., Mishra, S.R., Nguyen, V.V. and Liu, J.P. (2013) Synthesis and Characterization of High Coercivity Rare-Earth Ion Doped $Sr_{0.9}RE_{0.1}Fe_{10}Al_2O_{19}$ (RE: Y, La, Ce, Pr, Nd, Sm and Gd). *Journal of Alloys and Compounds*, **550**, 198-203. https://doi.org/10.1016/j.jallcom.2012.09.021

[24] Shannon, R.D. (1976) Revised Effective Ionic Radii and Systematic Studies of Interatomic Distances in Halides and Chalcogenides. *Acta Crystallographica Section A*: *Crystal Physics*, *Diffraction*, *Theoretical and General Crystallography*, **32**, 751-767. https://doi.org/10.1107/S0567739476001551

[25] Kambale, R.C., Shaikh, P.A., Kamble, S.S. and Kolekar, Y.D. (2009) Effect of Cobalt Substitution on Structural, Magnetic and Electric Properties of Nickel Ferrite. *Journal of Alloys and Compounds*, **478**, 599-603. https://doi.org/10.1016/j.jallcom.2008.11.101

[26] Ajroudi, L., Villain, S., Madigou, V., Mliki, N. and Leroux, C. (2010) Synthesis and Microstructure of Cobalt Ferrite Nanoparticles. *Journal of Crystal Growth*, **312**, 2465-2471. https://doi.org/10.1016/j.jcrysgro.2010.05.024

[27] Wang, L., Rai, B.K. and Mishra, S.R. (2015) Structural and Magnetic Study of Al^{3+} Doped $Ni_{0.75}Zn_{0.25}Fe_{2-x}Al_xO_4$ Nanoferrites. *Materials Research Bulletin*, **65**, 183-194. https://doi.org/10.1016/j.materresbull.2015.01.033

[28] Rezlescu, N., Doroftei, C., Rezlescu, E. and Popa, P.D. (2008) The Influence of Heat-Treatment on Microstructure and Magnetic Properties of Rare-Earth Substituted $SrFe_{12}O_{19}$. *Journal of Alloys and Compounds*, **451**, 492-496. https://doi.org/10.1016/j.jallcom.2007.04.102

[29] Lechevallier, L., Le Breton, J.M., Morel, A. and Tenaud, P. (2008) On the Solubility of Rare Earths in M-Type $SrFe_{12}O_{19}$ Hexaferrite Compounds. *Journal of Physics*: *Condensed Matter*, **20**, Article ID: 175203. https://doi.org/10.1088/0953-8984/20/17/175203

[30] Verma, V., Beniwal, A., Ohlan, A. and Tripathi, R. (2015) Structural, Magnetic and Ferroelectric Properties of Pr Doped Multiferroics Bismuth Ferrites. *Journal of Magnetism and Magnetic Materials*, **394**, 385-390. https://doi.org/10.1016/j.jmmm.2015.06.067

[31] Kong, S., Zhang, P., Wen, X., Pi, P., Cheng, J., Yang, Z. and Hai, J. (2008) Influence of Surface Modification of $SrFe_{12}O_{19}$ Particles with Oleic Acid on Magnetic Microsphere Preparation. *Particuology*, **6**, 185-190. https://doi.org/10.1016/j.partic.2008.03.004

[32] Kingery, W.D., Bowen, H.K. and Uhlmann, D.R. (1976) Introduction to Ceramics. John Willey and Sons, New York, 135-144.

[33] Nandotaria, R.A., Jotania, R.B., Sandhu, C.S., Hashim, M., Meena, S.S., Bhatt, P. and Shirsath, S.E. (2018) Magnetic Interactions and Dielectric Dispersion in Mg Substituted M-Type Sr-Cu Hexaferrite Nanoparticles Prepared Using One Step Solvent Free Synthesis Technique. *Ceramics International*, **44**, 4426-4435. https://doi.org/10.1016/j.ceramint.2017.12.043

[34] Rathod, V., Anupama, A.V., Kumar, R.V., Jali, V.M. and Sahoo, B. (2017) Correlated Vibrations of the Tetrahedral and Octahedral Complexes and Splitting of the Absorption Bands in FTIR Spectra of Li-Zn Ferrites. *Vibrational Spectroscopy*, **92**, 267-272. https://doi.org/10.1016/j.vibspec.2017.08.008

[35] Ansari, M.M.N., Khan, S. and Ahmad, N. (2018) Effect of R^{3+} (R = Pr, Nd, Eu and Gd) Substitution on the Structural, Electrical, Magnetic and Optical Properties of Mn-Ferrite Nanoparticles. *Journal of Magnetism and Magnetic Materials*, **465**, 81-87. https://doi.org/10.1016/j.jmmm.2018.05.071

[36] Pereira, F.M.M., Santos, M.R.P., Sohn, R.S.T.M., Almeida, J.S., Medeiros, A.M.L., Costa, M.M. and Sombra, A.S.B. (2009) Magnetic and Dielectric Properties of the M-Type Barium Strontium Hexaferrite ($Ba_xSr_{1-x}Fe_{12}O_{19}$) in the RF and Microwave (MW) Frequency Range. *Journal of Materials Science: Materials in Electronics*, **20**, 408-417. https://doi.org/10.1007/s10854-008-9744-8

[37] Li, C.J., Huang, B.N. and Wang, J.N. (2013) Effect of Aluminum Substitution on Microstructure and Magnetic Properties of Electrospun $BaFe_{12}O_{19}$ Nanofibers. *Journal of Materials Science*, **48**, 1702-1710. https://doi.org/10.1007/s10853-012-6928-7

[38] Stoner, E.C. and Wohlfarth, E.P. (1948) A Mechanism of Magnetic Hysteresis in Heterogeneous Alloys. *Philosophical Transactions of the Royal Society A, Mathematical and Physical Sciences*, **204**, 599-642. https://doi.org/10.1098/rsta.1948.0007

[39] Sahu, R.K., Mohanta, O. and Pramanik, A.K. (2012) XPS Study on the Correlation of Magnetic Properties and Site Occupancy of Al Doped $SrFe_{12}O_{19}$. *Journal of Alloys and Compounds*, **532**, 114-120. https://doi.org/10.1016/j.jallcom.2011.11.049

[40] Najafabadi, A.H., Mozaffarinia, R. and Ghasemi, A. (2015) Microstructural Characteristics and Magnetic Properties of Al-Substituted Barium Hexaferrite Nanoparticles Synthesized by Auto-Combustion Sol-Gel Processing. *Journal of Superconductivity and Novel Magnetism*, **28**, 2821-2830. https://doi.org/10.1007/s10948-015-3119-1

[41] Albanese, G., Carbucicchio, M. and Deriu, A. (1973) Substitution of Fe^{3+} by Al^{3+} in the Trigonal Sites of M-Type Hexagonal Ferrites. *Il Nuovo Cimento B* (1971-1996), **15**, 147-158. https://doi.org/10.1007/BF02894778

[42] Verwey, E.J.W. and De Boer, J.H. (1936) Cation Arrangement in a Few Oxides with Crystal Structures of the Spinel Types. *Recueil des Travaux Chimiques des Pays-Bas*, **55**, 531-540. https://doi.org/10.1002/recl.19360550608

[43] Shaikh, A.M., Bellad, S.S. and Chougule, B.K. (1999) Temperature and Frequency-Dependent Dielectric Properties of Zn Substituted Li-Mg Ferrites. *Journal of Magnetism and Magnetic Materials*, **195**, 384-390. https://doi.org/10.1016/S0304-8853(99)00138-9

[44] Nikumbh, A.K., Pawar, R.A., Nighot, D.V., Gugale, G.S., Sangale, M.D., Khanvilkar, M.B. and Nagawade, A.V. (2014) Structural, Electrical, Magnetic and Dielectric Properties of Rare-Earth Substituted Cobalt Ferrites Nanoparticles Synthesized by the Co-Precipitation Method. *Journal of Magnetism and Magnetic Materials*, **355**, 201-209. https://doi.org/10.1016/j.jmmm.2013.11.052

[45] Inbanathan, S.S.R., Vaithyanathan, V., Chelvane, J.A., Markandeyulu, G. and Bharathi, K.K. (2014) Mössbauer Studies and Enhanced Electrical Properties of R (R = Sm, Gd and Dy) Doped Ni Ferrite. *Journal of Magnetism and Magnetic Materials*, **353**, 41-46. https://doi.org/10.1016/j.jmmm.2013.10.019

[46] Maxwell, J.C. (1973) Electric and Magnetism. Oxford University Press, New York.

[47] Koops, C.G. (1951) On the Dispersion of Resistivity and Dielectric Constant of Some Semiconductors at Audio Frequencies. *Physical Review*, **83**, 121. https://doi.org/10.1103/PhysRev.83.121

[48] Narang, S.B., Singh, A. and Singh, K. (2007) High Frequency Dielectric Behavior of Rare Earth Substituted Sr-M Hexaferrite. *Journal of Ceramic Processing Research*, **8**, 347.

[49] Melagiriyappa, E., Jayanna, H.S. and Chougule, B.K. (2008) Dielectric Behavior and AC Electrical Conductivity Study of Sm^{3+} Substituted Mg-Zn Ferrites. *Materials Chemistry and Physics*, **112**, 68-73. https://doi.org/10.1016/j.matchemphys.2008.05.014

[50] Ali, I., Islam, M.U., Awan, M.S., Ahmad, M. and Iqbal, M.A. (2013) Structural, Electrical and Microstructure Properties of Nanostructured Calcium Doped Ba-Hexaferrites Synthesized by Sol-Gel Method. *Journal of Superconductivity and Novel Magnetism*, **26**, 3277-3286. https://doi.org/10.1007/s10948-013-2167-7

[51] Pervaiz, E. and Gul, I.H. (2012) Structural, Electrical and Magnetic Studies of Gd^{3+} Doped Cobalt Ferrite Nanoparticles. *International Journal of Current Engineering and Technology*, **2**, 377-387.